iScience

Article

Cerenkov luminescence microscopy: A novel approach for high-resolution radiotracer imaging

Graphical abstract

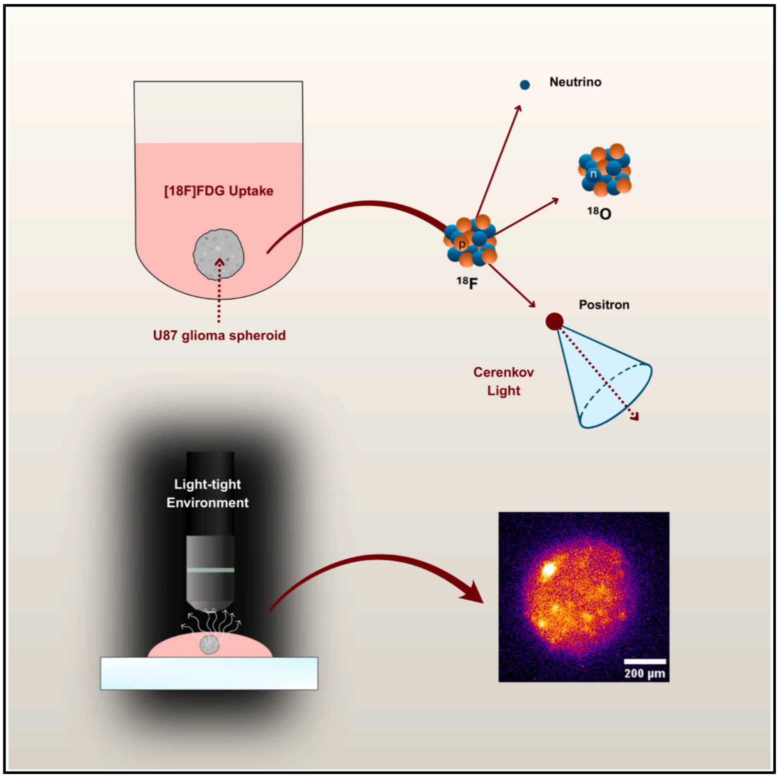

Highlights

- Evaluation of a novel imaging technique: Cerenkov luminescence microscopy
- Successful testing with [18F]FDG on human glioblastoma spheroid models
- Technique optimization may enable new advances in personalized medicine

Authors

Lisa Alborghetti, Federica Vurro,
Sara Belloli, ..., Rosa Maria Moresco,
Federico Boschi, Antonello Enrico Spinelli

Correspondence

spinelli.antonello@hsr.it

In brief

Medical imaging; Applied sciences

Alborghetti et al., 2025, iScience *28*, 113840
November 21, 2025 © 2025 The Author(s). Published by Elsevier Inc.
https://doi.org/10.1016/j.isci.2025.113840

CellPress

iScience

CellPress
OPEN ACCESS

Article

Cerenkov luminescence microscopy: A novel approach for high-resolution radiotracer imaging

Lisa Alborghetti,[1,2] Federica Vurro,[1] Sara Belloli,[3,7] Paolo Rainone,[3,7] Silvia Valtorta,[3,7,8] Macrina Milani Capialbi,[1]
Maria Assunta Lacavalla,[1,5] Stefano Pizzardi,[1] Rosa Maria Moresco,[4,7,8] Federico Boschi,[6]
and Antonello Enrico Spinelli[1,9,*]
[1]IRCCS San Raffaele Scientific Institute, Experimental Imaging Center, Milano 20132, Italy
[2]University of Verona, Department of Diagnostics and Public Health, Verona 37134, Italy
[3]CNR, Institute of Bioimaging and Biological Complex Systems (IBSBC), Segrate 20054, Italy
[4]Bicocca University, Department of Medicine and Surgery, Monza, Italy
[5]University of Padova, Department of Chemical Sciences, Padova 35131, Italy
[6]University of Verona, Department of Engineering for Innovation Medicine, Verona 37134, Italy
[7]IRCCS San Raffaele Scientific Institute, Nuclear Medicine Unit, Milano 20132, Italy
[8]University of Milano-Bicocca, GBM-BI-TRACE (GlioBlastoMa-BIcocca-TRAnslational-CEnter), Monza, Italy
[9]Lead contact
*Correspondence: spinelli.antonello@hsr.it
https://doi.org/10.1016/j.isci.2025.113840

SUMMARY

This study introduces a novel imaging system utilizing Cerenkov luminescence microscopy (CLM) to visualize the activity of radioactive tracers in 3D tumor spheroids. The system integrates an EMCCD camera, a microscope objective, and a precise sample positioning setup, enabling the high-resolution detection of Cerenkov light emission from radiotracers in a light-tight environment. The characteristics of the new CLM system have been tested on glioblastoma multiforme (GLM) spheroids, subjected or not to X-ray radiotherapy. The system effectively differentiated irradiated from non-irradiated spheroids by detecting distinct variations in signal intensity, which were further validated through comparison with autoradiography and quantitative activity measurements. This demonstrates the system's ability to provide highly sensitive imaging of radiolabeled biological samples. The method offers new possibilities for studying radiopharmaceutical distribution and metabolic processes at the cellular level, making it a valuable tool for advancing both diagnostic and therapeutic radiopharmaceutical development, as well as for evaluating treatment efficacy.

INTRODUCTION

Cerenkov luminescence imaging (CLI) is an optical imaging technique that exploits the emission of Cerenkov radiation. This phenomenon occurs when charged particles travel through a dielectric medium at a velocity greater than the phase velocity of light in that medium. The passage of these high-energy particles induces a transient polarization of the surrounding medium, which subsequently releases energy in the form of photons as they return to equilibrium.[1,2] Unlike conventional optical imaging methods, CLI harnesses this intrinsic light emission, eliminating the need for external excitation sources. CLI has shown significant potential in both diagnostic and therapeutic applications. In the context of radionuclide decay, the emitted charged particles can generate Cerenkov light, effectively converting decay energy into visible, detectable photons. This enables non-invasive, real-time imaging of radiotracer distribution, with applications ranging from tumor localization to monitoring therapeutic responses. Because it bridges nuclear medicine and optical imaging, CLI provides a valuable tool for accurate cancer detection, image-guided interventions, and potentially theranostics.[3] Despite some limitations, such as low light output and limited penetration depth, CLI has been proposed for a range of applications in both preclinical and clinical settings. The majority of these involve the use of radiopharmaceuticals administered to small animals or patients,[4–10] while others explore Cerenkov luminescence as a quality assurance tool in radiotherapy.[11–13] A key limitation of CLI is the strong absorption of Cerenkov radiation in the UV/blue spectrum by biological tissues, which restricts its effectiveness in living organisms. Innovative approaches, such as the integration of ultrasmall downconverting nanoparticles, have been explored to shift Cerenkov emission toward longer, more penetrative wavelengths and improve *in vivo* imaging performance.[14–18] Future efforts will likely aim at enhancing image resolution and depth penetration while broadening CLI's applications in clinical settings. In this study, we investigated the feasibility of adapting CLI methodologies to achieve high-resolution imaging of radiopharmaceutical distribution within three-dimensional (3D) tumor spheroids, which, compared to conventional two-dimensional (2D) cell cultures, replicate more closely the structural and physiological characteristics of *in vivo* tumors, providing a more realistic experimental

© 2025 The Author(s). Published by Elsevier Inc.
This is an open access article under the CC BY-NC license (http://creativecommons.org/licenses/by-nc/4.0/).

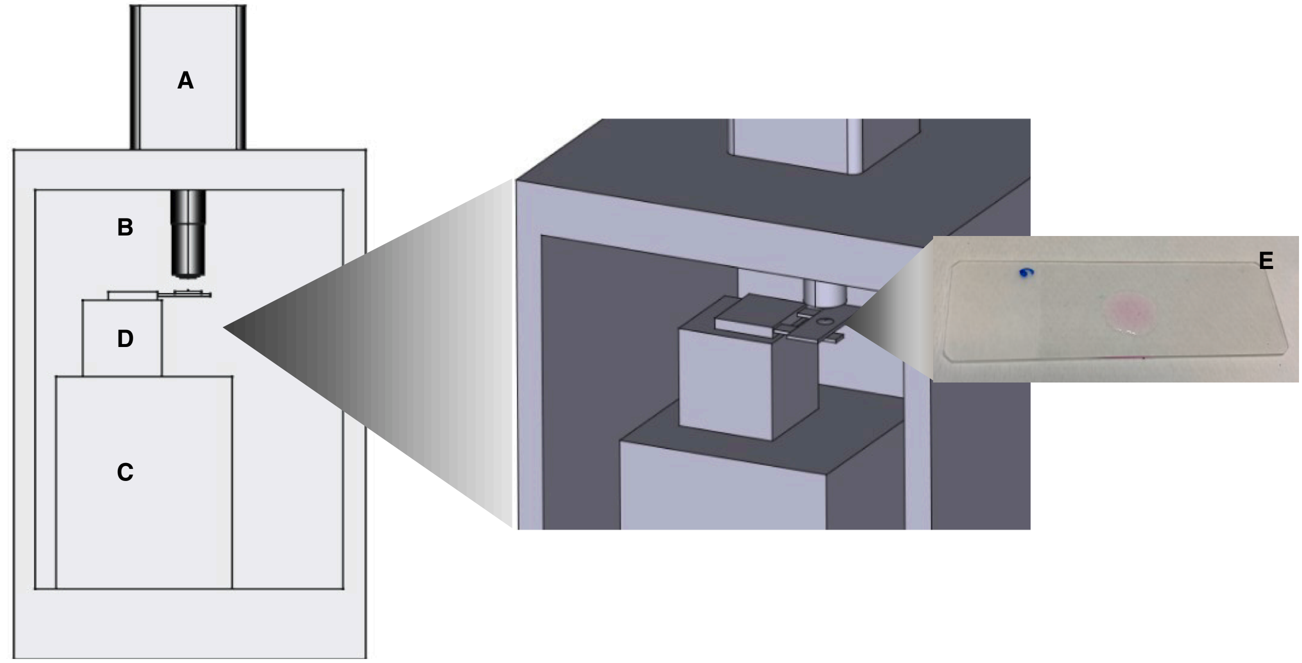

Figure 1. CLM system setup

The system features an Andor EMCCD camera (A) mounted on the top of a black plexiglass enclosure. A 20×/0.45 microscope objective (B) is coupled to the camera for imaging. The sample, placed on a microscope slide (E), is positioned and focused using a coarse z axis stage (C) and a three-axis micrometric positioning system (D). The enclosure is sealed with a hermetic door and further covered with a light-tight fabric to prevent external light interference.

system.[19–21] To address this, we developed a novel microscopy approach based on Cerenkov luminescence, termed Cerenkov luminescence microscopy (CLM), enabling visualization and analysis of radiopharmaceutical uptake and distribution at the spheroid level. This method involves administering a radiopharmaceutical to the spheroids and allowing sufficient time for cellular uptake and distribution of the radiotracer. As the unstable nuclei of the radioactive element in the compound undergo radioactive decay (most commonly resulting in the emission of a positron (β^+) or electron (β^-) from the nucleus), the emitted charged particles travel through the spheroid and its medium. In this way, if the kinetic energy of the particles exceeds the threshold for Cerenkov photon production, the spheroid itself acts as a Cerenkov radiator. The resulting light serves as an intrinsic signal, directly reflecting the radiopharmaceutical distribution and uptake mechanisms within the spheroid. β decay is a three-body process, meaning that the emitted electrons or positrons do not have a single discrete energy for a given isotope but instead follow a continuous energy spectrum. Despite this, each isotope can be characterized by key parameters, such as its average β energy and its endpoint energy, which represents the maximum kinetic energy of the emitted particle. Isotopes with higher endpoint β energies are particularly advantageous for Cerenkov imaging, as they produce a stronger optical signal. However, this increased energy also results in longer trajectories for the β particles, leading to a greater spatial dispersion of the emitted Cerenkov light. This trade-off must be carefully considered when selecting isotopes for imaging. In the first part of this study, we described a prototype microscope for CLM and characterized its performance using a sealed ^{22}Na radioactive source. For the same scope, we also compared the Cerenkov signals generated by two different β^+ emitters, ^{18}F and ^{68}Ga, which have distinct endpoint energies (634 keV and 1899 keV, respectively). Following this, we experimentally demonstrated the feasibility of CLM for imaging tumor spheroids using [^{18}F]Fluorodeoxyglucose ([^{18}F]FDG), the most widely used diagnostic radiopharmaceutical,[22] and compared the results with different techniques, including gamma counting, autoradiography, and radioluminescence microscopy (RLM).[23,24] Our findings highlight the potential of the proposed method as an effective approach for supporting the development of diagnostic and therapeutic radiopharmaceuticals and for evaluating treatment efficacy using 3D tumor models.

RESULTS

Imaging system description and characterization

The experimental setup consisted of a light-tight box equipped with an EMCCD back-illuminated 512 × 512 sensor camera (Andor iXon Ultra 897 EMCCD), coupled with an interchangeable extension tube and a microscope objective. Inside the box, a positioning system allowed precise focusing of samples on a microscope slide (Figure 1). A removable LED light could be positioned under the sample and used for bright field imaging and focusing of the examined material. With a 60 mm c-mount extension tube and a 20×/0.45 microscope objective, the effective pixel size was determined to be 1.6 μm, and the field of view was around 800 × 800 μm.[2] A characterization of the system

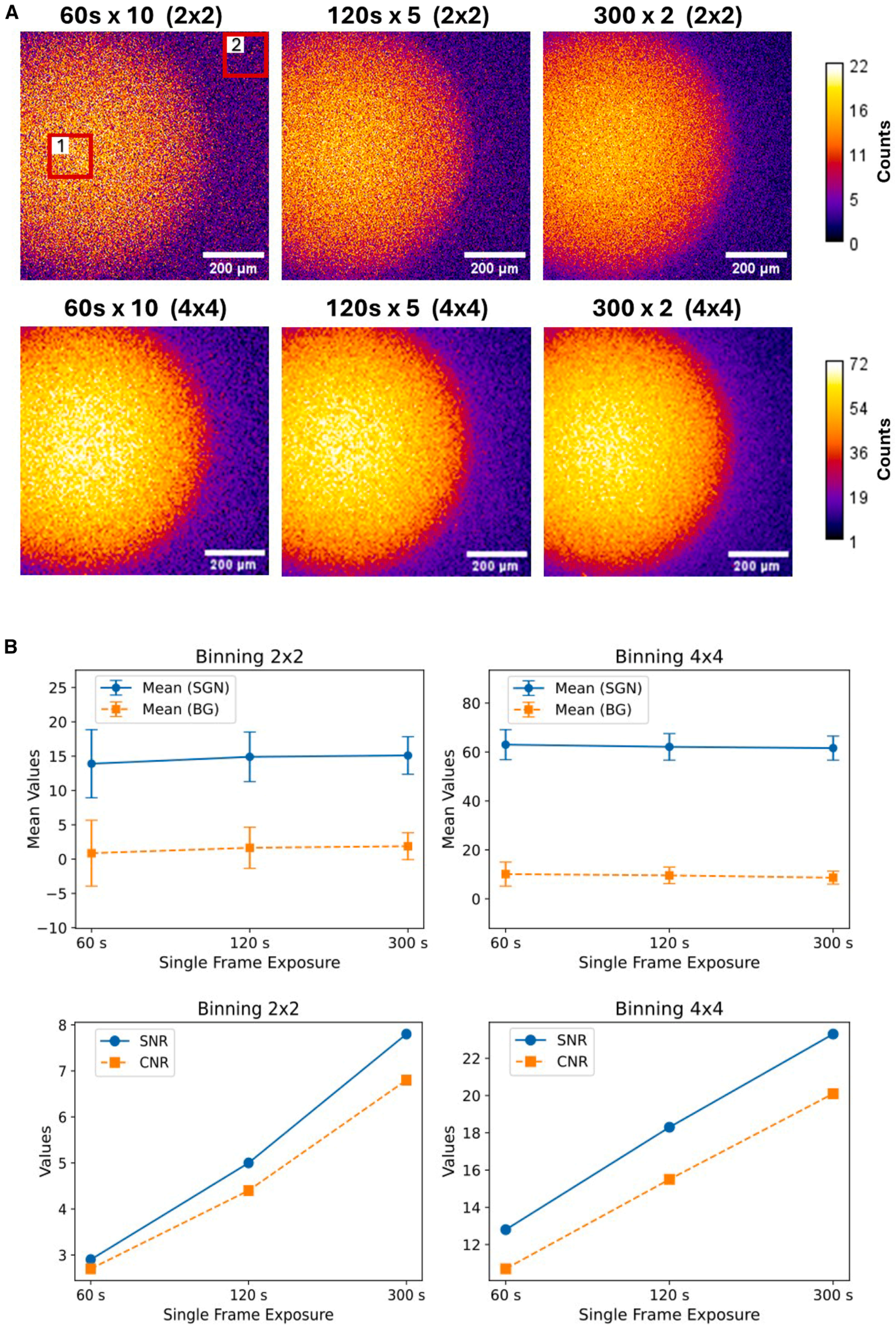

(legend on next page)

point spread function (PSF) and modulation transfer function (MTF) is provided in the supplemental information (Figure S1). The settings of the detector can be modified via a software interface (Andor Solis software platform). Among the most important options, it is possible to choose the desired exposure duration, the most suitable binning value, and the temperature of the detector (up to -100°C). For all the CLM measurements, the detector was maintained at -80°C, and the CCD operated in conventional mode, deliberately disabling EM amplification to avoid increasing reading noise. As discussed in Section evaluation of optimal exposure time to a ^{22}Na radioactive source, the imaging technique we propose requires long exposure times, which result in low frames per second (FPS). Under such conditions, EM gain would amplify both dark current and noise, ultimately degrading image quality. Similarly, high readout frequencies are unnecessary; therefore, all CLM images were acquired at a readout frequency of 80 kHz.

Evaluation of optimal exposure time to a ^{22}Na radioactive source

A spherical radioactive source of ^{22}Na was used to determine the optimal exposure time for CLM. The source, with a nominal diameter of 1 mm, was encased within a 2 mm thick plexiglass slab. ^{22}Na is a β^+ emitter with a main endpoint energy of 547 keV, closely matching the endpoint energy of ^{18}F (634 keV). The nominal activity of the source is 37 kBq, which is consistent with the activity measured during preliminary evaluations of [^{18}F]FDG uptake in spheroids, approximately 50–100 kBq (the methods for [^{18}F]FDG administration and uptake in spheroids are described in the STAR Methods section). Consequently, despite inherent differences in the optical properties of the materials and the geometrical conditions, the Cerenkov signal emitted by the source is expected to be comparable to that emitted by spheroids. This makes the ^{22}Na source suitable for optimizing the imaging protocol, particularly benefiting from the stability of its activity ($\tau_{1/2} = 2.6019$ years). Image sequences with a total exposure time of 10 min were acquired using different frame rates: 10 frames with 60 s exposure, 5 frames with 120 s exposure, and 2 frames with 300 s exposure (Figure 2). Corrections for bias, background, and dark current removal were applied to each frame of the series before summing them. The signal-to-noise ratio (SNR) and contrast-to-noise ratio (CNR) of the resulting images were then evaluated and compared. The results indicate that a longer exposure is preferable, as it yields higher SNR and CNR values.

Comparison between ^{18}F and ^{68}Ga

As previously discussed, different radionuclides with varying decay modes and endpoint energies can generate distinct Cerenkov signals. To explore these differences, we compared by CLM and Monte Carlo simulations the Cerenkov signal of ^{18}F with that of ^{68}Ga, another clinically relevant β^+ emitter,[25,26] which has an endpoint energy approximately three times higher than that of ^{18}F (1.899 MeV). Two glass capillaries, each with an internal diameter of 1 mm, were filled with 2 μL of ^{68}Ga-chloride and [^{18}F]FDG, respectively. The capillaries were positioned under a 10× microscope objective, with the field of view covering their entire width. This setup enabled the imaging of the Cerenkov signal emitted by both the radiopharmaceuticals and the surrounding glass. Images were captured with an exposure time of 5 min per sample (Figure 3A). The ratio of the maximum observed signal intensity between ^{68}Ga-chloride and [^{18}F]FDG, normalized to the activity at the beginning of the exposure, was approximately 6.5 (Figure 3B). For comparison, the experiment's geometry was simulated using the TOPAS Monte Carlo simulation tool.[27,28] In this simulation, the ratio of optical photons detected at the outer curved surface of the cylindrical capillary for ^{68}Ga versus ^{18}F was approximately 10. Simulated images were also generated by scoring the coordinates of the Cerenkov photons that reached the x-z plane, which intersects the capillary at its midpoint. The simulated images are shown in Figure 3C. A comparison between the signals from CLM images and Monte Carlo simulated images for the two radionuclides is shown in Figure 3D. The results of Monte Carlo simulations for additional radionuclides used in diagnostic, therapeutic, and theranostic applications are available in the supplemental information (Figures S4 and S5).

Cerenkov luminescence microscopy first applications: imaging of irradiated spheroids

Ten spheroids were seeded in a 96 multi-well round bottom plate. On day 2 after seeding, five spheroids were irradiated with a 20 Gy dose of X-rays using the Small Animal Radiation Research Platform (SmART, PXI) available at our research facility. The remaining five spheroids constituted the control group. On day 7, CLM was performed on five irradiated (RT) and five controls (CTRL) spheroids to assess the presence of discernible differences between the two groups. Ten spheroids were seeded in a 96-well round-bottom plate. On day 2 after seeding, five spheroids were irradiated with a 20 Gy dose of X-rays using the Small Animal Radiation Research Platform (SmART, PXI) available at our research facility. The remaining five spheroids constituted the control group. On day 7, CLM was performed on five irradiated (RT) and five control (CTRL) spheroids to assess the presence of discernible differences between the two groups. For each spheroid, two consecutive frames of 5 min were acquired and subsequently summed during image analysis, resulting in a total effective exposure time of 10 min per spheroid. After the

Figure 2. ^{22}Na CLM images at different exposure times and binning

(A) Comparison of ^{22}Na images acquired using Cerenkov luminescence microscopy (CLM) with different exposure times and binning settings (scale bars = 200 μm). A total exposure time of 10 min was achieved, summing 10 frames with 60 s exposure each (left), 5 frames with 120 s exposure each (center), and 2 frames with 300 s exposure each (right). The displayed images represent the sum of the acquired frames. Images in the first row were processed with binning 2, while those in the second row used binning 4. Square sections 1 and 2 in the first image indicate the regions of interest (ROIs) selected for signal and background analysis, respectively. These ROIs were used to calculate the signal-to-noise ratio (SNR) and contrast-to-noise ratio (CNR), with the corresponding results presented in the graphs later in discussion (B). Data in the top row of (b) graphs are represented as the mean value of the signal in the selected ROI ± standard deviation.

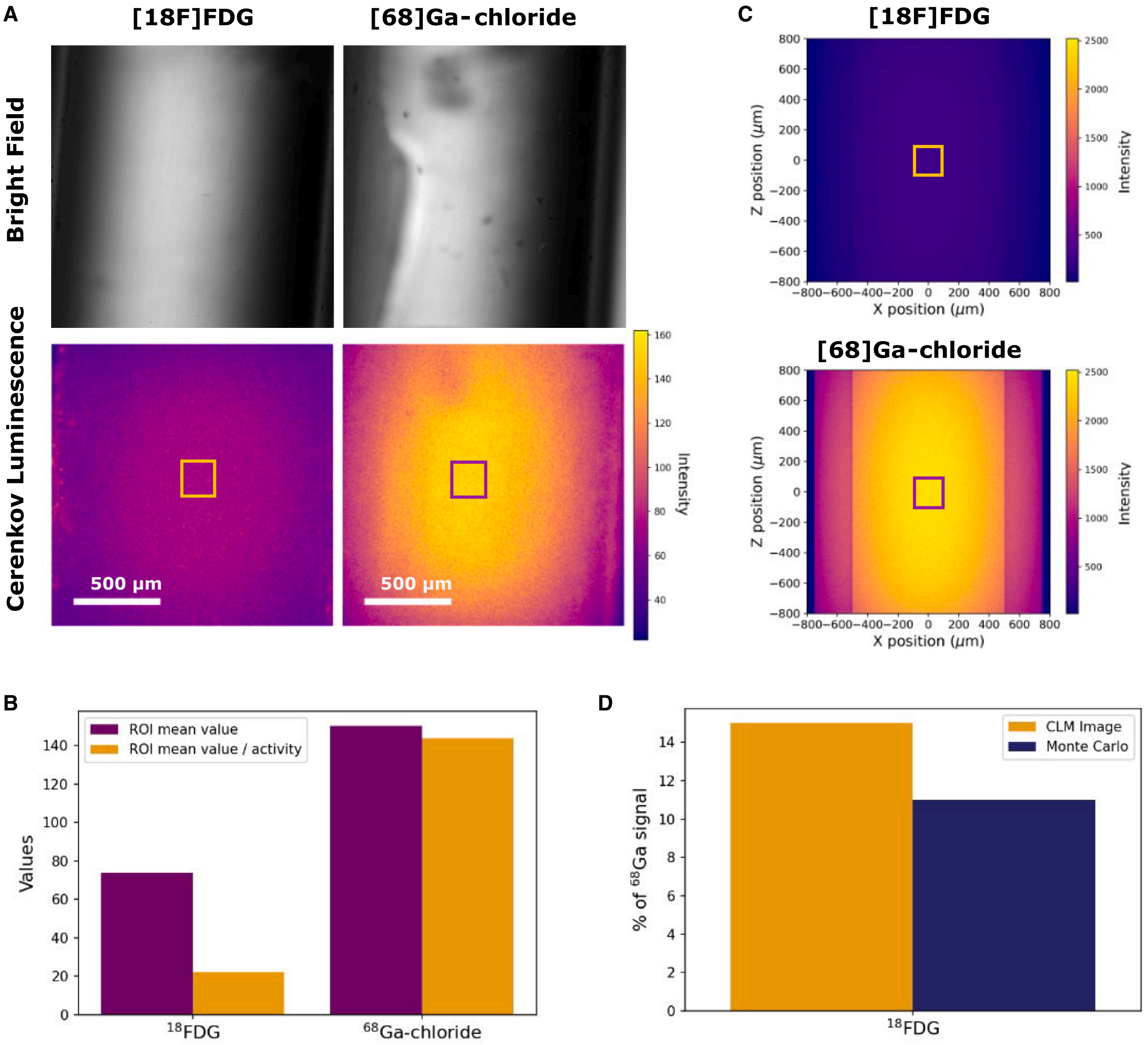

Figure 3. Comparison between [^{18}F]FDG and ^{68}Ga-chloride in glass capillaries

(A) Bright field and Cerenkov luminescence microscopy (CLM) images of two 1 mm internal diameter capillaries containing 2 μL of [^{18}F]FDG and ^{68}Ga-chloride. CLM images were obtained using a 10× microscope objective. Exposure time = 300 s, temperature = −80°C, binning = 2×2, effective pixel size = 3.2 μm, scale bars = 500 µm.

(B) Plot shows the average pixel values computed in two ROIs on the CLM images displayed in panel (a). The purple bars represent the raw pixel values, while the orange bars correspond to the normalized values obtained by dividing the raw values by the activity *A(t)* at the time *t* when the image acquisition began.

(C) Images show the simulated Cerenkov photon distribution on the x-z plane, bisecting the capillary. The photon count was generated using a TOPAS Monte Carlo simulation, based on 10^7 volumetrically distributed decay events within the capillary. A more detailed description of the simulation is given in supplemental information (Figure S3).

(D) Plot compares the percentage values of the [^{18}F]FDG signal relative to the ^{68}Ga-chloride signal in both CLM images and Monte Carlo simulated images. The reference values used for the Monte Carlo simulation are the average pixel values calculated from the ROIs on the images shown in panel (C).

imaging, radioactivity measurements, and autoradiography were performed on the same spheroids. A timeline of the experiment is shown in Figure 4A, and the effect of RT on spheroids' size is shown in Figures 4B and 4C. The spheroids [^{18}F]FDG uptake was evaluated with a γ-counter at the end of CLM acquisitions, by correcting for radioisotope decay. Once the activity of all the spheroids had been established, a simultaneous autoradiography of all samples was carried out using a Cyclone Phosphor Imager (PerkinElmer), with a film exposure time of 1 min. It should be noted that [^{18}F]FDG uptake was performed one spheroid at a

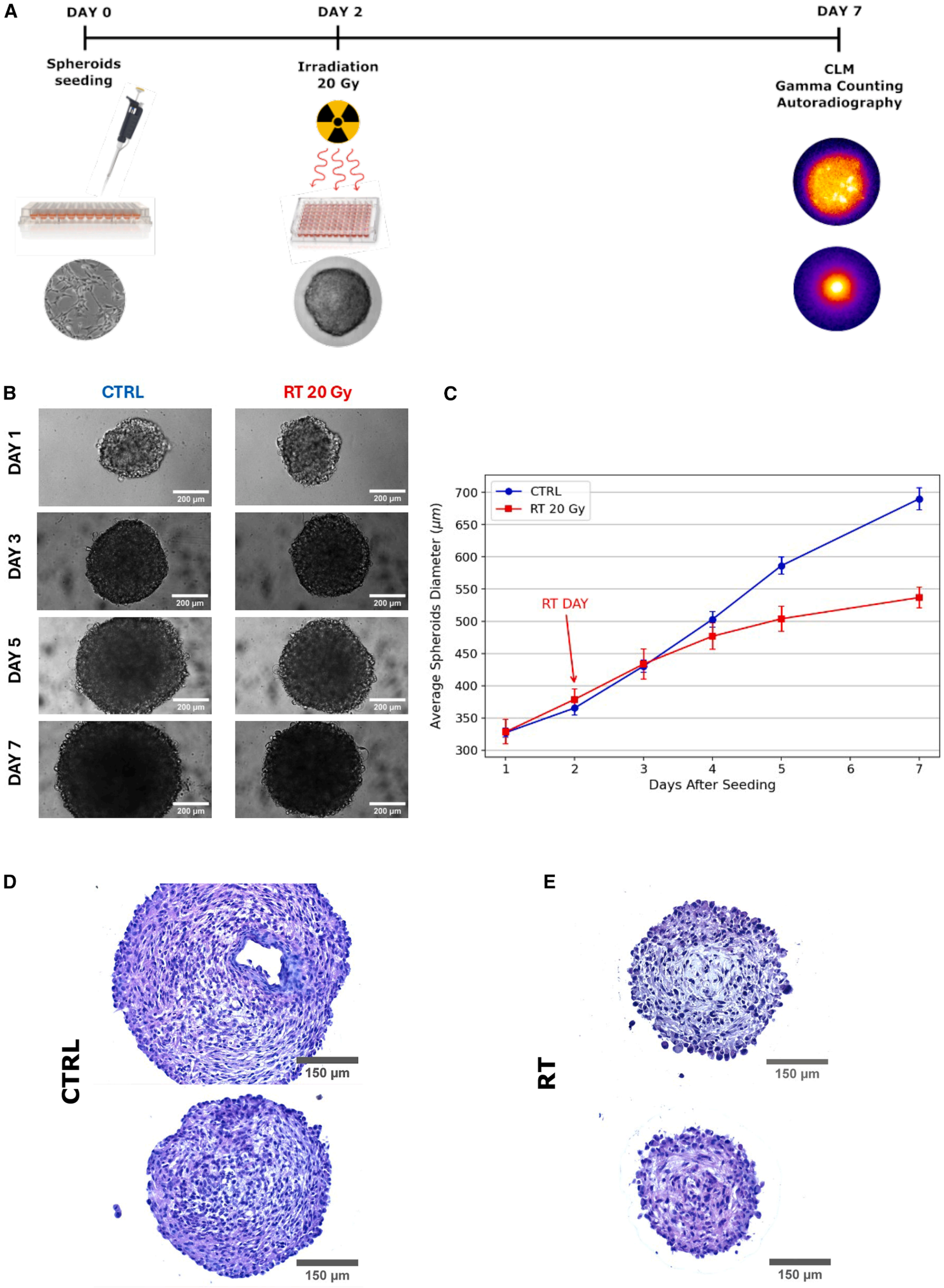

(legend on next page)

time, with approximately 20 min of delay between each. This sequential approach ensured an efficient workflow and allowed imaging to be conducted under consistent conditions across all samples. As a result, each spheroid was imaged after approximately the same time from the end of the uptake, making it unnecessary to apply ^{18}F decay corrections. Given the relatively short half-life of ^{18}F ($\sim$110 min), this is a crucial aspect to consider. Figure 5A presents the resulting images of the ten analyzed spheroids, shown in both bright field and CLM. All CLM images were generated by adding two consecutive acquisitions, each with an exposure time of 5 min. To enhance the signal, 2×2 binning was applied, resulting in images with dimensions of 256×256 pixels (effective pixel size = 3.2 μm). Further details on image processing are provided in the STAR Methods. The boxplots in Figure 6A summarize the data obtained from image analysis, including the spheroid area, mean signal per pixel, and total integrated signal across the spheroid. The average integrated signal for CTRL and RT was $(8.1 \pm 0.8) \times 10^5$ counts and $(3.9 \pm 0.3) \times 10^5$ counts, respectively, with a CTRL-to-RT ratio of 2.1 ± 0.3. Additionally, data on the radioactivity of spheroids are reported in Figure 6B. The average radioactivity at t = 0 (immediately after the end of the [^{18}F]FDG uptake) resulted in 113 ± 5 kBq for the CTRL group and 56 ± 5 kBq for the RT group (ratio = 2.0 ± 0.2). A one-sided Mann-Whitney U test was performed on these quantities, revealing statistically significant differences between CTRL and RT for all parameters: spheroid area, mean signal per pixel, and integrated signal (p = 0.004), as well as spheroid activity (p = 0.008). The outcome of the autoradiography is presented in Figures 5B and 6C. The integrated signal was calculated for each spheroid, accounting for the varying time intervals between the end of the uptake phase and autoradiography acquisition. The average integrated signal is $(1.4 \pm 0.3) \times 10^8$ and $(0.8 \pm 0.3) \times 10^8$ for the CTRL and RT groups, respectively. The CTRL-to-RT ratio of the average integrated signal was 1.7 ± 0.7, consistent with the activity ratio measured from the γ-counter for the two groups. Furthermore, the one-sided Mann-Whitney U test performed on the integrated signal of CTRL and RT spheroids revealed statistically significant differences (p = 0.016) between the two groups. The results of all three methods.

(CLM, activity measurements, and autoradiography) show good correlation, as represented in figure (6 days).

H&E staining of irradiated and non-irradiated spheroids

Histological sections of irradiated and non-irradiated spheroids, fixed on day 7 and stained with hematoxylin and eosin (H&E), are shown in Figures 4D and 4E. Control spheroids, which are larger in size, display a prominent central necrotic area, a characteristic found in more voluminous three-dimensional structures, surrounded by a peripheral rim of viable cells. In irradiated spheroids, a marked reduction in overall cellularity is observed, with fewer visible nuclei, indicating a cytotoxic effect of radiotherapy and resulting in a less compact architecture compared to controls. In addition to differences in size and necrotic core, hematoxylin and eosin staining highlights further morphological alterations between groups. Control spheroids display a compact peripheral rim of viable cells with densely packed nuclei, while the central necrotic area is characterized by eosinophilic amorphous material and loss of cellular detail. In irradiated spheroids, nuclei appear less numerous and, in some cases, pyknotic or fragmented, consistent with treatment-induced cell death. The overall tissue architecture is looser, with wider intercellular spaces and a reduced nuclear-to-cytoplasmic ratio, while cytoplasmic eosinophilia and occasional vacuolization further indicate cellular damage. These features collectively support a cytotoxic effect of radiotherapy and a disruption of spheroid organization. Additional images of spheroid sections are provided in the supplemental information, along with representative images of U87 cells grown in 2D cultures, which closely reflect the features observed in spheroids (Figures S6–S8).

Comparison between radioluminescence microscopy and Cerenkov luminescence microscopy imaging of spheroids

The system's capability to perform radioluminescence microscopy (RLM) was evaluated and compared to CLM imaging. Following the procedure described in the STAR Methods section, [^{18}F]FDG uptake by a single spheroid was achieved. A glass equipped with a 0.3 mm-thick plastic ring was used (Figures 7A and 7B). The spheroid was placed inside the ring, and CLM was performed (temperature: −80°C, exposure: 300 s, binning: 4×4). Immediately after, a CaF_2(Eu) scintillator disk (diameter = 20 mm, thickness = 0.5 mm) was positioned onto the plastic ring to avoid flattening of the spheroid, and an image with the same acquisition setting was acquired (a comparison of different scintillators used for imaging the ^{22}Na source is provided in the supplemental information, Figure S2). Figures 7C and 7D show a comparison between the two obtained images. Quantitative analysis revealed that the average signal within a 20×20 pixel region of interest (ROI) centered on the spheroid was approximately 75 times higher in the RLM image compared to the CLM image. However, normalized intensity profiles demonstrated that CLM provided superior delineation of spheroid margins and better detection of signal inhomogeneities compared to RLM (Figure 7E).

Figure 4. Experimental timeline and U87 spheroids characterization

(A) Timeline of the experiment. DAY 0: U87 human glioblastoma cells were seeded into ultralow attachment round-bottom 96-well plates. DAY 2: A 20 Gy X-ray dose was administered to a group of spheroids. DAY 7: Cerenkov luminescence microscopy (CLM), γ-counting, and autoradiography were performed on both irradiated and non-irradiated spheroids.

(B) Comparison of images showing groups of control (CTRL) and irradiated (RT 20 Gy, two days after seeding) U87 spheroids at 1-, 3-, 5-, and 7-days post-seeding. Scale bars = 200 μm.

(C) Trend in diameter growth for CTRL and RT spheroids. Each data point represents the average diameter of 12 spheroids, with error bars indicating the standard deviation.

(D and E) Representative H&E-stained sections of CTRL and RT spheroids. RT samples were irradiated on day 2, and all spheroids were fixed on day 7. Scale bars = 150 μm.

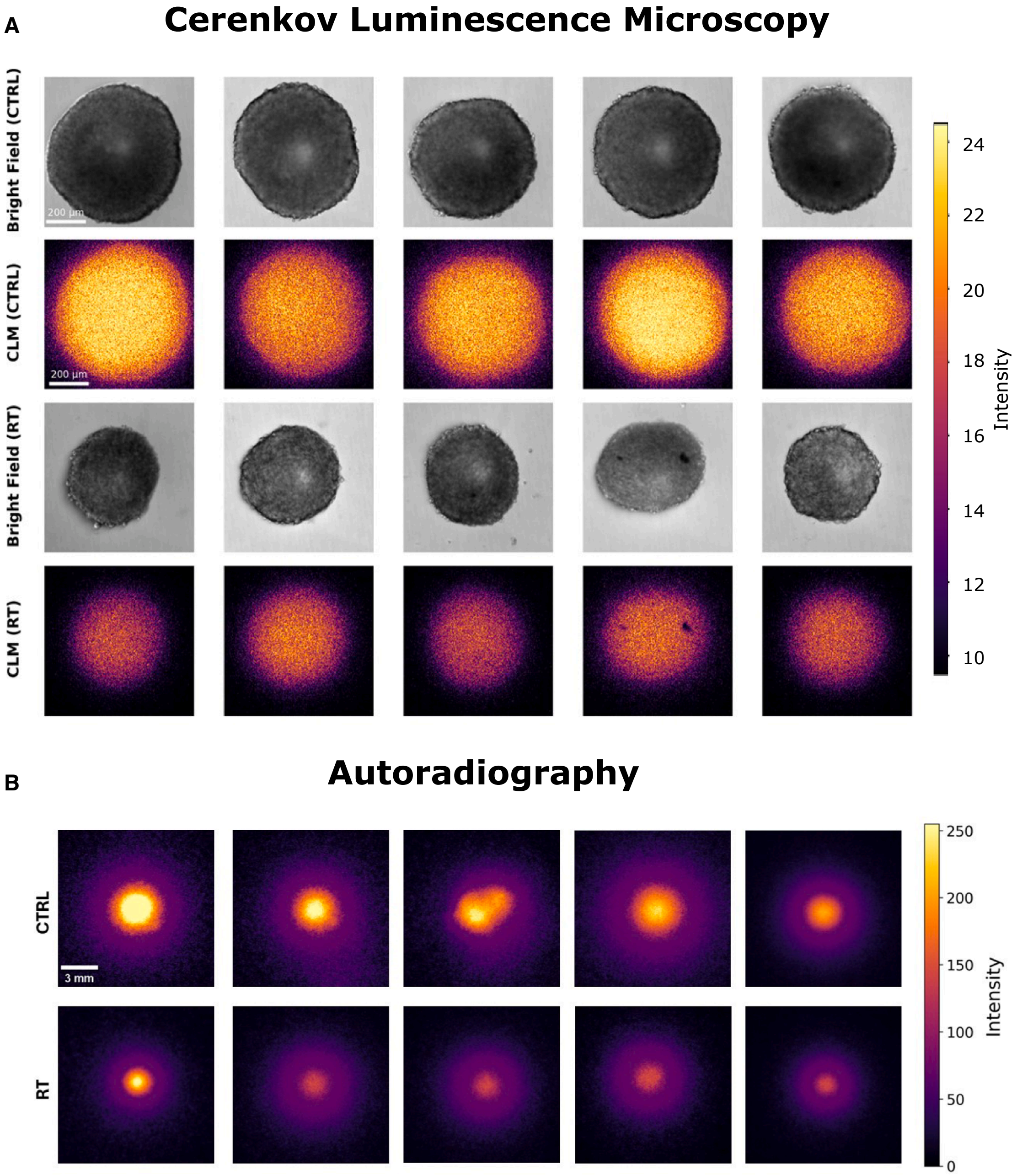

Figure 5. CLM and autoradiography of irradiated and non-irradiated spheroids

(A) Images of two groups of spheroids (CTRL = controls, RT = 20 Gy X-ray radiotreated), shown in both bright field and Cerenkov luminescence microscopy (CLM). Imaging was performed five days after the delivery of the RT. All CLM images were obtained by summing two consecutive acquisitions, each with an exposure time of 5 min. To enhance the signal, 2×2 binning was applied (image size = 256×256 px, effective pixel size = 3.2 μm, scale bars = 200 μm).

(B) Autoradiography of the same CTRL and RT spheroids. The autoradiographic film was exposed for 1 min. From the overall autoradiography image, individual 300 × 300 pixel regions corresponding to each spheroid were extracted (effective pixel size = 42 μm, scale bars = 3 mm). The signal from each spheroid was then adjusted using an exponential correction to account for the varying time intervals between the end of the uptake phase and autoradiography acquisition. Note the considerably different spatial scales of the CLM and autoradiography images, reflecting their respective resolutions and fields of view.

Inhomogeneities in spheroids

Some of the acquired CLM images revealed notable inhomogeneities in signal intensity, with regions exhibiting brightness levels up to three times higher than the average signal of the spheroid. Examples of this distinctive behavior are shown in Figure 8. A similar pattern was observed in bioluminescence microscopy (BLM) images of a separate set of glioblastoma spheroids, as shown in Figure 8, where such signal inhomogeneities

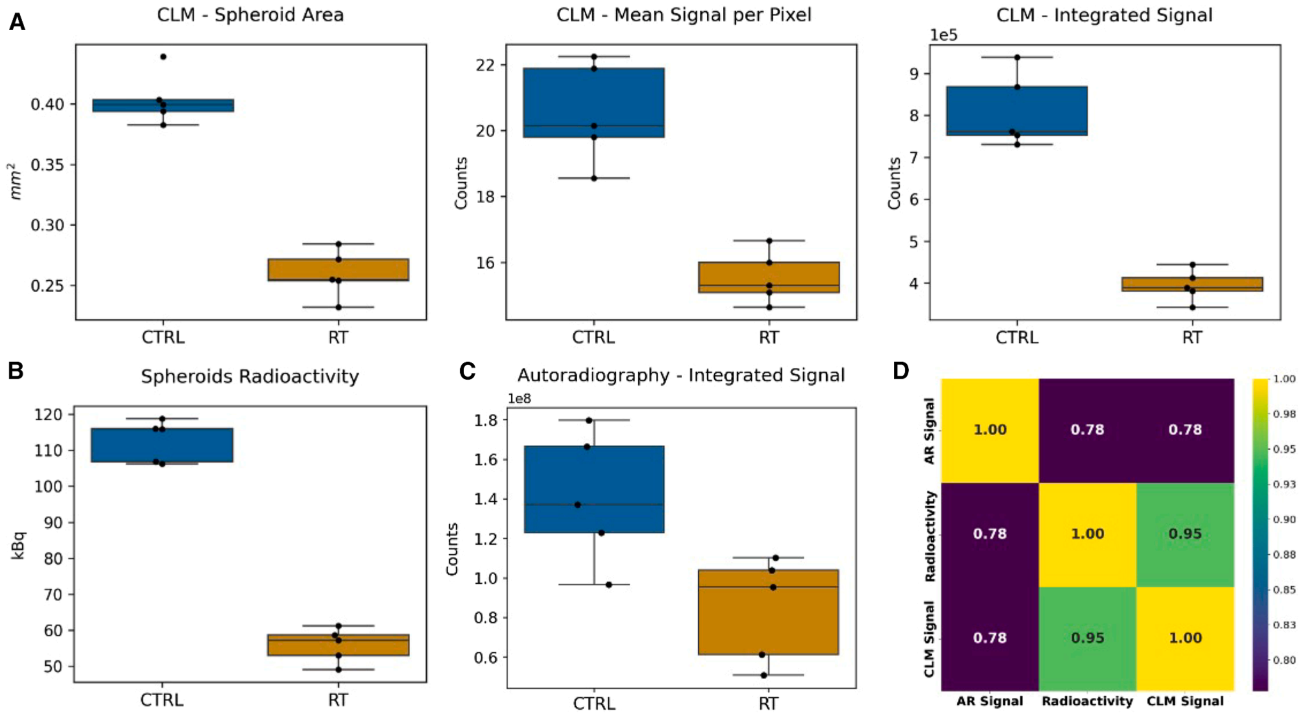

Figure 6. Quantitative analysis and correlations between CLM, γ-counter, and autoradiography

(A) Boxplots derived from the analysis of Cerenkov luminescence microscopy (CLM) images of irradiated (RT) and non-irradiated (CTRL) glioblastoma spheroids. The CLM image analysis included measurements of the two-dimensional (2D) area [mm^2], the average signal per pixel, and the integrated signal across the entire 2D spheroid area.

(B) Spheroids radioactivity [kBq] at the start of CLM acquisition.

(C) Time-corrected integrated signal for the autoradiography. In all boxplots shown in (A), (B), and (C), the box represents the interquartile range (from the first to the third quartile), the black line inside the box indicates the median value, and the whiskers denote the minimum and maximum values.

(D) Matrix of the correlation coefficients for the measurements obtained with CLM (CLM Signal), γ-counter (Radioactivity), and autoradiography (AR Signal). A very good correlation (0.95) is obtained between Radioactivity and CLM Signal, while a lower but still good correlation (0.78) is observed between AR Signal and the other two methods. All the correlation coefficients resulted in statistically significant (Pearson p-value < 0.02).

frequently appeared in both irradiated and non-irradiated samples. Bioluminescence imaging, which relies on the detection of light emitted by specific biochemical reactions, provides a non-invasive method to visualize cellular activity.[29,30] Notably, the conditions required for performing BLM - primarily a dark environment and high detector sensitivity - are the same as those for CLM, making our instrument suitable for both techniques. The procedure used to perform BLM is detailed in STAR Methods.

DISCUSSION

In this study, we demonstrated the feasibility of adapting Cerenkov luminescence imaging (CLI) methodologies for high-resolution microscopy of Cerenkov radiation emitted from [^{18}F]FDG in 3D tumor spheroids. The obtained Cerenkov luminescence microscopy (CLM) signal correlated well with the radioactivity of the spheroids, as confirmed by comparison with a gold-standard technique such as γ-counting. A similar agreement was observed with autoradiography, where the integrated signal closely matched the CLM measurements. While autoradiography is faster and enables the simultaneous processing of multiple samples, its major limitation lies in the spatial resolution of the imaging approach. As shown in Figure 5, the spatial scale of the autoradiography images is more than ten times coarser than that of CLM, which directly affects both resolution and field of view. In contrast, CLM delivers far more detailed images, providing markedly superior spatial resolution and enabling the detection of spatial inhomogeneity in signal distribution within the spheroid. Importantly, these irregularities were also observed with bioluminescence microscopy (BLM) on the same type of spheroids. Nevertheless, it is crucial to underline that the two techniques are based on different principles: CLM reflects the uptake of radiopharmaceuticals within the spheroid, while BLM derives from a biochemical reaction (luciferase–luciferin) in the presence of cells expressing the luciferase gene and is therefore not related to any radiopharmaceutical uptake mechanism. For this reason, the two modalities provide similar (e.g., presence of tumor cells) but not directly comparable information. The biological origin of the irregularities detected by CLM, and also visible with BLM, remains to be further investigated.

Although RLM provides a stronger and less noisy signal than CLI, the resulting images are considerably blurrier. This effect

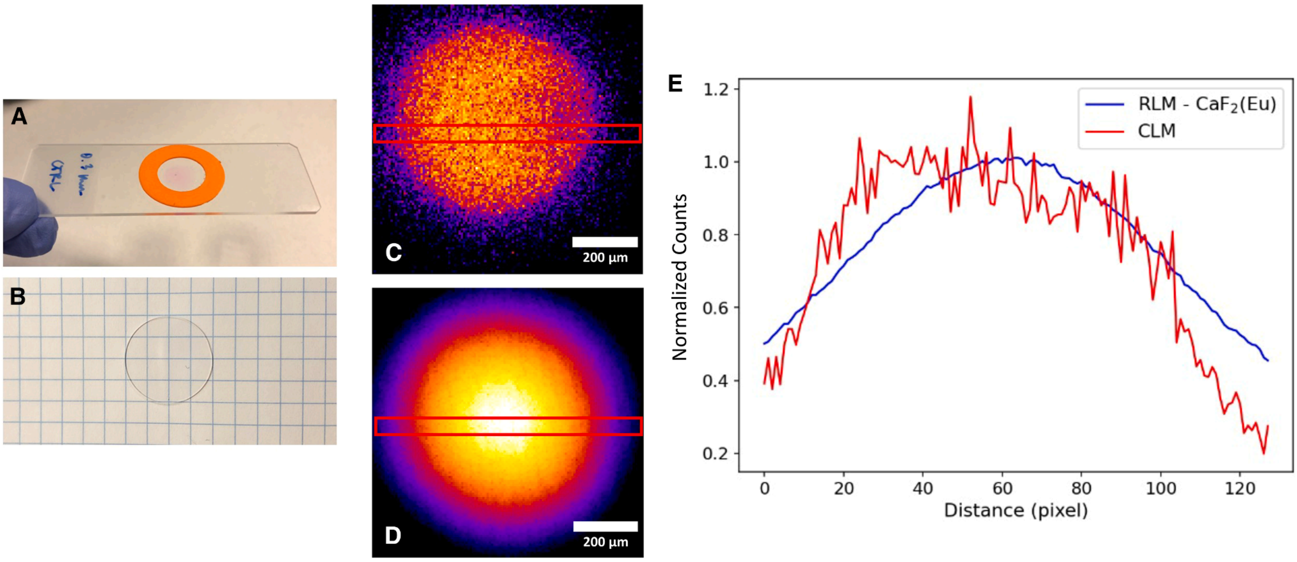

Figure 7. Comparison between CLM and RLM imaging of a spheroid

(A) A 0.3 mm-thick plastic ring was placed on a microscope slide, with a spheroid positioned inside the ring. A thin CaF_2(Eu) scintillator disk (B) was then placed on top of the ring for radioluminescence microscopy (RLM).

(C) Cerenkov luminescence microscopy (CLM) image of a spheroid.

(D) Radioluminescence microscopy (RLM) image of the same spheroid. For both images, the scale bars are 200 μm. The acquisition parameters for CLM and RLM images were: exposure time = 300 s, binning = 4 × 4, and CCD temperature = -80°C. Average horizontal intensity profiles measured within the red ROIs highlighted in (c) for CLM and in (D) for RLM are shown on the (E) panel (ROI dimensions = 128×8 pixels).

arises from the way the RLI signal is generated: the scintillating light spreads extensively within the scintillator slab,[31] much more than the Cerenkov light. We believe that, despite its lower light yield and higher noise level, CLM offers a sharper representation of the actual radioactivity distribution within spheroids. By contrast, RLM images appear markedly blurred and homogeneous, potentially masking underlying heterogeneities.

A comparison of the CLM signals from ^{68}Ga and ^{18}F revealed differences in Cerenkov light production, reflecting variations in positron endpoint energies. These findings are broadly consistent with previously reported results in the literature.[32,33] Monte Carlo simulation results were also reasonably consistent with the experimental measurements, even if the simulated images are simplified models of the real, more complex system optics. Future studies should investigate how variations in radioisotope emissions influence imaging quality when applied to spheroid models. It should be noted that these simulations consider only Cerenkov photons; however, additional - albeit weaker - sources of optical emission resulting from radioactive decay have been demonstrated, including fluorescence and radioluminescence induced in the medium by charged particles and gamma rays.[34–37] When imaging radioisotopes that induce a weak or absent Cerenkov signal, these alternative emissions could, in principle, serve as detectable sources. Nonetheless, in such cases, radioluminescence imaging using scintillators would generally offer a more suitable approach.

The proposed technique holds significant potential for various applications, such as drug screening and development, by enabling the use of the same radiopharmaceuticals synthesized for human imaging, thereby providing more translationally relevant results. Unlike fluorescence imaging, which requires the development of specifically labeled molecules, Cerenkov imaging does not rely on additional labeling. This allows, in principle, the visualization of any radiopharmaceutical without the need to design a dedicated probe.

While in this work we concentrated on glucose metabolism using [^{18}F]FDG, future studies will explore the potential of this approach to investigate more specific biomarkers. In particular, radiotracers such as [^{18}F]FLT for assessing tumor proliferation or [^{18}F]FET for monitoring amino acid transport, both widely used in nuclear medicine for PET imaging,[38–40] could provide valuable insights into spheroid biology and further demonstrate the versatility of the system. Notably, β emitters and diagnostic radiopharmaceuticals are not the only suitable candidates for Cerenkov luminescence microscopy: although α particles do not generate Cerenkov radiation directly, this technique can still be applied to α-emitting radionuclides due to the presence of β-emitting daughter isotopes within their decay chains. Thus, CLM could also facilitate translational large-scale drug screening, provide insights into the therapeutic efficacy of many drug candidates, and contribute to dosimetry optimization as well as a better understanding of drug interactions within the tumor microenvironment.

Further research should explore CLM applications in more complex *in vitro* systems, including multicell-type spheroids, co-cultures, and patient-derived organoids, which more accurately replicate tumor biology. In addition, testing CLM with different cancer types characterized by variable [^{18}F]FDG avidity

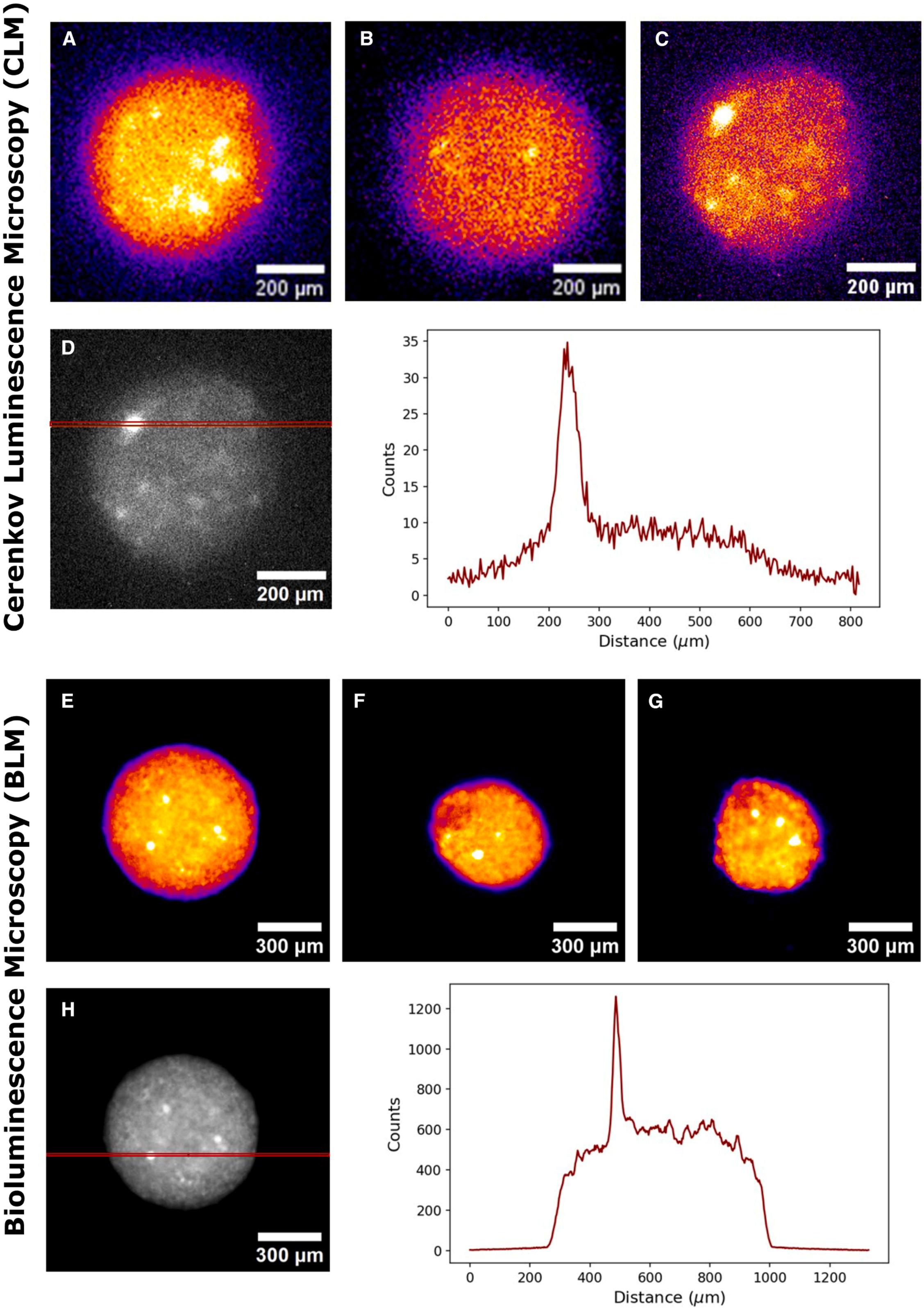

(legend on next page)

or differential uptake of specific radiopharmaceuticals would further validate its versatility and broaden its translational potential. Investigating CLM in these advanced models could expand its role in preclinical research by enabling precise radiotracer evaluation and supporting both personalized treatment strategies and the development of novel nuclear medicine probes for imaging and therapy.

It is worth noting that the reported results were obtained using a prototype instrument and should therefore be regarded as a proof-of-principle demonstration. This work represents only the first step of a broader path that will involve progressive refinement of the technique, optimization of the instrumentation, and a more in-depth exploration of its full potential. Enhancements such as a more stable and versatile positioning system, as well as an objective with a higher numerical aperture, would help minimize blurring and maximize photon collection. Given the inherently low efficiency of Cerenkov emission, preserving as many optical photons as possible is crucial to maintaining a detectable signal. Additionally, improvements in image reconstruction software could significantly enhance resolution and contrast. Advanced computational techniques, such as deconvolution algorithms, denoising filters, and machine-learning-based image enhancement, offer promising solutions to address challenges arising from optical distortions and the intrinsically weak Cerenkov signal intensity, allowing the extraction of meaningful insights from this emerging microscopy technique. Future technological developments could further extend CLM's capabilities, enabling three-dimensional imaging through approaches such as z stack acquisition, tomographic reconstruction, and advanced volumetric analysis. Furthermore, the development of scanning-based 2D techniques could enable the detailed study of other types of biological specimens, including thin tissue slices, thereby broadening the scope of CLM beyond spheroids and reinforcing its potential as a versatile preclinical imaging tool.

Limitations of the study

- The results presented in this work were obtained using a prototype instrument. Further technical optimization is expected to improve image quality.
- Cerenkov luminescence microscopy was tested on a single cell line only. Future work will extend the investigation to additional cell lines and to more complex 3D tumor models, to better assess the robustness and generalizability of the technique.
- The technique was evaluated exclusively with FDG as a radiopharmaceutical. Testing with other clinically relevant radiotracers, will be important to explore its broader applicability.

RESOURCE AVAILABILITY

Lead contact

Requests for further information and resources should be directed to and will be fulfilled by the lead contact, Antonello Spinelli (spinelli.antonello@hsr.it).

Materials availability

This study did not generate new unique reagents.

Data and code availability

- All data reported in this article will be shared with the lead contact upon request.
- This article does not report the original code.
- Any additional information required to reanalyze the data reported in this article is available from the lead contact upon request.

ACKNOWLEDGMENTS

The research leading to these results has received funding from AIRC under IG 2022, ID. 27336, project PI: Antonello E. Spinelli. The authors thank Dr. Maria Grazia Minotti and Pasquale Simonelli of San Raffaele Scientific Institute for [^{18}F]FDG production and handling.

AUTHOR CONTRIBUTIONS

Data curation, formal analysis, investigation, software, visualization, and writing – original draft, L.A.; investigation, methodology, and writing – original draft, F.V.; investigation, methodology, supervision, and writing – review and editing, S.B.; investigation and methodology, P.R. and S.V.; investigation, M.M.C. and M.A.L.; investigation and writing – review and editing, S.P.; resources and supervision, R.M.M.; supervision and writing – review and editing, F.B.; conceptualization, funding acquisition, project administration, supervision, and writing – review and editing, A.E.S.

DECLARATION OF INTERESTS

The authors declare no competing interests.

STAR★METHODS

Detailed methods are provided in the online version of this paper and include the following:

- KEY RESOURCES TABLE
- EXPERIMENTAL MODEL AND STUDY PARTICIPANT DETAILS
    - ○ Cell line and spheroids culture
- METHOD DETAILS
    - ○ CLM sample preparation and imaging
    - ○ BLM sample preparation and imaging
    - ○ Spheroids paraffin inclusion, sectioning and staining
- QUANTIFICATION AND STATISTICAL ANALYSIS
    - ○ Spheroids activity evaluation
    - ○ Image processing
    - ○ Image features quantification and statistics
    - ○ Signal-to-noise and contrast-to-noise ratios
    - ○ Monte Carlo simulations of Cerenkov emission

Figure 8. Signal inhomogeneities in the CLM and BLM of spheroids

On the top, Cerenkov light microscopy images of non-irradiated glioblastoma spheroids. (A–C) panels show images obtained with a 300 s exposure time and binning 4×4 (A) or 2×2 (B and C). A 20× magnification objective was used, corresponding to an effective pixel size of 3.2 μm. Brighter spots are visible, and panel (D) shows the average horizontal intensity profile extracted from the highlighted red ROI (256 × 4 pixels). The profile reveals a peak with a full width at half maximum (FWHM) of approximately 40 μm. In the bottom panel, bioluminescence microscopy (BLM) images of non-irradiated (E) and irradiated (F and G) glioblastoma spheroids. The three panels show images obtained with a 10 s exposure time. No binning was applied. A 10× magnification objective was used, corresponding to an effective pixel size of 2.6 μm. Similarly to CLM images, brighter spots are visible, with panel (H) displaying the average horizontal intensity profile from the evidenced red ROI (512 × 4 pixels). In this case, the profile shows a peak with FWHM of approximately 20 μm.

SUPPLEMENTAL INFORMATION

Supplemental information can be found online at https://doi.org/10.1016/j.isci.2025.113840.

Received: June 6, 2025
Revised: September 1, 2025
Accepted: October 18, 2025
Published: October 24, 2025

REFERENCES

1. Cherenkov, P.A. (1967). Visible Glow under Exposure of Gamma Radiation. Uspekhi Fizicheskih Nauk *93*, 385–388. https://doi.org/10.3367/UFNr.0093.196710n.0385.
2. Tamm, I.E., and Frank, I.M. (1967). Coherent visible radiation of fast electrons passing through matter. Uspekhi Fizicheskih Nauk *93*, 388–393. https://doi.org/10.3367/UFNr.0093.196710o.0388.
3. Teng, M., Liang, X., Liu, H., Li, Z., Gao, X., Zhang, C., Cheng, H., Chen, H., and Liu, G. (2024). Cerenkov radiation shining a light for cancer theranostics. Nano Today *55*, 102174. https://doi.org/10.1016/j.nantod.2024.102174.
4. Spinelli, A.E., Kuo, C., Rice, B.W., Calandrino, R., Marzola, P., Sbarbati, A., and Boschi, F. (2011). Multispectral Cerenkov luminescence tomography for small animal optical imaging. Opt. Express *19*, 12605. https://doi.org/10.1364/OE.19.012605.
5. Spinelli, A.E., Ferdeghini, M., Cavedon, C., Zivelonghi, E., Calandrino, R., Fenzi, A., Sbarbati, A., and Boschi, F. (2013). First human Cerenkography. J. Biomed. Opt. *18*, 020502. https://doi.org/10.1117/1.JBO.18.2.020502.
6. Galiè, M., Boschi, F., Scambi, I., Merigo, F., Marzola, P., Altabella, L., Lavagnolo, U., Sbarbati, A., and Spinelli, A.E. (2017). Theranostic Role of ^{32}P-ATP as Radiopharmaceutical for the Induction of Massive Cell Death within Avascular Tumor Core. Theranostics *7*, 4399–4409. https://doi.org/10.7150/thno.21403.
7. Mc Larney, B.E., Zhang, Q., Pratt, E.C., Skubal, M., Isaac, E., Hsu, H.T., Ogirala, A., and Grimm, J. (2023). Detection of Shortwave-Infrared Cerenkov Luminescence from Medical Isotopes. J. Nucl. Med. *64*, 177–182. https://doi.org/10.2967/jnumed.122.264079.
8. Tamura, R., Pratt, E.C., and Grimm, J. (2018). Innovations in Nuclear Imaging Instrumentation: Cerenkov Imaging. Semin. Nucl. Med. *48*, 359–366. https://doi.org/10.1053/j.semnuclmed.2018.02.007.
9. Xu, Y., Liu, H., and Cheng, Z. (2011). Harnessing the Power of Radionuclides for Optical Imaging: Cerenkov Luminescence Imaging. J. Nucl. Med. *52*, 2009–2018. https://doi.org/10.2967/jnumed.111.092965.
10. Boschi, F., Calderan, L., D'Ambrosio, D., Marengo, M., Fenzi, A., Calandrino, R., Sbarbati, A., and Spinelli, A.E. (2011). In vivo 18F-FDG tumour uptake measurements in small animals using Cerenkov radiation. Eur. J. Nucl. Med. Mol. Imaging *38*, 120–127. https://doi.org/10.1007/s00259-010-1630-y.
11. Helo, Y., Rosenberg, I., D'Souza, D., MacDonald, L., Speller, R., Royle, G., and Gibson, A. (2014). Imaging Cerenkov emission as a quality assurance tool in electron radiotherapy. Phys. Med. Biol. *59*, 1963–1978. https://doi.org/10.1088/0031-9155/59/8/1963.
12. Glaser, A.K., Zhang, R., Gladstone, D.J., and Pogue, B.W. (2013). Projection imaging of photon beams using Cerenkov-excited fluorescence. Phys. Med. Bio. *58*, 601–619. https://doi.org/10.1088/0031-9155/58/3/601.
13. Glaser, A.K., Zhang, R., Gladstone, D.J., and Pogue, B.W. (2014). Optical dosimetry of radiotherapy beams using Cherenkov radiation: the relationship between light emission and dose. Phys. Med. Biol. *59*, 3789–3811. https://doi.org/10.1088/0031-9155/59/14/3789.
14. Pratt, E.C., Shaffer, T.M., and Grimm, J. (2016). Nanoparticles and radiotracers: advances toward radionanomedicine. WIREs Nanomed. Nanobiotechnol. *8*, 872–890. https://doi.org/10.1002/wnan.1402.
15. Zhang, Q., Pratt, E.C., Tamura, R., Ogirala, A., Hsu, H.T., Farahmand, N., O'Brien, S., and Grimm, J. (2021). Ultrasmall Downconverting Nanoparticle for Enhanced Cerenkov Imaging. Nano Lett. *21*, 4217–4224. https://doi.org/10.1021/acs.nanolett.1c00049.
16. Thorek, D.L.J., Ogirala, A., Beattie, B.J., and Grimm, J. (2013). Quantitative imaging of disease signatures through radioactive decay signal conversion. Nat. Med. *19*, 1345–1350. https://doi.org/10.1038/nm.3323.
17. Genovese, D., Petrizza, L., Prodi, L., Rampazzo, E., De Sanctis, F., Spinelli, A.E., Boschi, F., and Zaccheroni, N. (2020). Tandem Dye-Doped Nanoparticles for NIR Imaging via Cerenkov Resonance Energy Transfer. Front. Chem. *8*, 71. https://doi.org/10.3389/fchem.2020.00071.
18. Boschi, F., and Spinelli, A.E. (2020). Nanoparticles for Cerenkov and Radioluminescent Light Enhancement for Imaging and Radiotherapy. Nanomaterials *10*, 1771. https://doi.org/10.3390/nano10091771.
19. Baker, B.M., and Chen, C.S. (2012). Deconstructing the third dimension – how 3D culture microenvironments alter cellular cues. J. Cell Sci. *125*, 3015–3024. https://doi.org/10.1242/jcs.079509.
20. Weiswald, L.-B., Bellet, D., and Dangles-Marie, V. (2015). Spherical Cancer Models in Tumor Biology. Neoplasia *17*, 1–15. https://doi.org/10.1016/j.neo.2014.12.004.
21. Zhao, Z., Chen, X., Dowbaj, A.M., Sljukic, A., and Bratlie, K. (2022). Organoids. Nat. Rev. Methods Primers *2*, 94. https://doi.org/10.1038/s43586-022-00186-8.
22. Crisan, G., Moldovena-Cioroianu, N.S., Timaru, D.-G., Andries, G., Căinap, C., and Chis, V. (2022). Radiopharmaceuticals for PET and SPECT Imaging: A Literature Review over the Last Decade. Int. J. Mol. Sci. *23*, 5023. https://doi.org/10.3390/ijms23095023.
23. Pratx, G., Chen, K., Sun, C., Martin, L., Carpenter, C.M., Olcott, P.D., and Xing, L. (2012). Radioluminescence Microscopy: Measuring the Heterogeneous Uptake of Radiotracers in Single Living Cells. PLoS One *7*, e46285. https://doi.org/10.1371/journal.pone.0046285.
24. Khan, S., Shin, J.H., Ferri, V., Cheng, N., Noel, J.E., Kuo, C., Sunwoo, J.B., and Pratx, G. (2021). High-resolution positron emission microscopy of patient-derived tumor organoids. Nat. Commun. *12*, 5883. https://doi.org/10.1038/s41467-021-26081-6.
25. Bozkurt, M.F., Virgolini, I., Balogova, S., Beheshti, M., Rubello, D., Decristoforo, C., Ambrosini, V., Kjaer, A., Delgado-Bolton, R., Kunikowska, J., et al. (2017). Guideline for PET/CT imaging of neuroendocrine neoplasms with 68GaDOTA-conjugated somatostatin receptor targeting peptides and 18F–DOPA. Eur. J. Nucl. Med. Mol. Imaging *44*, 1588–1601. https://doi.org/10.1007/s00259-017-3728-y.
26. Banerjee, S.R., and Pomper, M.G. (2013). Clinical applications of Gallium-68. Appl. Radiat. Isot. *76*, 2–13. https://doi.org/10.1016/j.apradiso.2013.01.039.
27. Faddegon, B., Ramos-Mendez, J., Schuemann, J., McNamara, A., Shin, J., Perl, J., and Paganetti, H. (2020). The TOPAS tool for particle simulation, a Monte Carlo simulation tool for physics, biology and clinical research. Phys. Med. *72*, 114–121. https://doi.org/10.1016/j.ejmp.2020.03.019.
28. Perl, J., Shin, J., Schumann, J., Faddegon, B., and Paganetti, H. (2012). TOPAS: An innovative proton Monte Carlo platform for research and clinical applications. Med. Phys. *39*, 6818–6837. https://doi.org/10.1118/1.4758060.
29. Paley, M.A., and Prescher, J.A. (2014). Bioluminescence: a versatile technique for imaging cellular and molecular features. Medchemcomm *5*, 255–267. https://doi.org/10.1039/C3MD00288H.
30. Tung, J.K., Berglund, K., Gutekunst, C.-A., Hochgeschwender, U., and Gross, R.E. (2016). Bioluminescence imaging in live cells and animals. Neurophotonics *3*, 025001. https://doi.org/10.1117/1.NPh.3.2.025001.
31. Wang, Q., Sengupta, D., Kim, T.J., and Pratx, G. (2018). In silico optimization of radioluminescence microscopy. J. Biophotonics *11*, e201700138. https://doi.org/10.1002/jbio.201700138.
32. Pratt, E.C., Shaffer, T.M., Bauer, D., Lewis, J.S., and Grimm, J. (2023). Radiances of Cerenkov-Emitting Isotopes on the IVIS. Preprint at bioRxiv. https://doi.org/10.1101/2023.01.18.524625.

33. Beattie, B.J., Thorek, D.L.J., Schmidtlein, C.R., Pentlow, K.S., Humm, J.L., and Hielscher, A.H. (2012). Quantitative Modeling of Cerenkov Light Production Efficiency from Medical Radionuclides. PLoS One *7*, e31402. https://doi.org/10.1371/journal.pone.0031402.

34. Boschi, F., Meo, S.L., Rossi, P.L., Calandrino, R., Sbarbati, A., and Spinelli, A.E. (2011). Optical imaging of alpha emitters: simulations, phantom, and in vivo results. J. Biomed. Opt. *16*, 126011. https://doi.org/10.1117/1.3663441.

35. Boschi, F., De Sanctis, F., and Spinelli, A.E. (2018). Optical emission of^{223} Radium: in vitro and in vivo preclinical applications. J. Biophotonics *11*, e201700209. https://doi.org/10.1002/jbio.201700209.

36. Ackerman, N.L., Boschi, F., and Spinelli, A.E. (2017). Monte Carlo simulations support non-Cerenkov radioluminescence production in tissue. J. Biomed. Opt. *22*, 1–11. https://doi.org/10.1117/1.JBO.22.8.086002.

37. Spinelli, A.E., Lo Meo, S., Calandrino, R., Sbarbati, A., and Boschi, F. (2011). Optical imaging of Tc-99m–based tracers: in vitro and in vivo results. J. Biomed. Opt. *16*, 116023. https://doi.org/10.1117/1.3653963.

38. Holzgreve, A., Nitschmann, A., Maier, S.H., Büttner, M., Schönecker, S., Marschner, S.N., Fleischmann, D.F., Corradini, S., Belka, C., La Fougère, C., et al. (2024). FET PET-based target volume delineation for the radiotherapy of glioblastoma: A pictorial guide to help overcome methodological pitfalls. Radiother. Oncol. *198*, 110386. https://doi.org/10.1016/j.radonc.2024.110386.

39. Nikaki, A., Papadopoulos, V., Valotassiou, V., Efthymiadou, R., Angelidis, G., Tsougos, I., Prassopoulos, V., and Georgoulias, P. (2019). Evaluation of the Performance of 18F-Fluorothymidine Positron Emission Tomography/Computed Tomography (18F-FLT-PET/CT) in Metastatic Brain Lesions. Diagnostics *9*, 17. https://doi.org/10.3390/diagnostics9010017.

40. Brahm, C.G., Den Hollander, M.W., Enting, R.H., De Groot, J.C., Solouki, A.M., Den Dunnen, W.F.A., Heesters, M.A.A.M., Wagemakers, M., Verheul, H.M.W., De Vries, E.G.E., et al. (2018). Serial FLT PET imaging to discriminate between true progression and pseudoprogression in patients with newly diagnosed glioblastoma: a long-term follow-up study. Eur. J. Nucl. Med. Mol. Imaging *45*, 2404–2412. https://doi.org/10.1007/s00259-018-4090-4.

STAR★METHODS

KEY RESOURCES TABLE

REAGENT or RESOURCE	SOURCE	IDENTIFIER
Chemicals, peptides, and recombinant proteins		
Trypsin 0.25% EDTA	Life Technologies	#cat 25200072
VALUE FBS	Life Technologies	#cat a5256701
PFA 16% W/V AQ.SOL MEOH free 10×	Thermoscientific	#cat 11400580
DMEM high glucose GlutaMAX Supplement	Gibco	#cat 10566016
Penicillin-Streptomycin (10,000 U/ml)	gibco	#cat 15140148
Hematoxylin	Bio Optica	–
Eosin	Bio Optica	–
D-Luciferin Potassium Salt	Perkin Elmer	–
[18F]Fluorodeoxyglucose	IRCCS San Raffaele Scientific Institute	–
Experimental models: Cell lines		
U-87 MG luc+	IRCCS San Raffaele Scientific Institute	–
Software and algorithms		
Python	Python Version 3.8.20	Python Release Python 3.8.20 | Python.org
ImageJ	NIH	ImageJ 1.54f

EXPERIMENTAL MODEL AND STUDY PARTICIPANT DETAILS

Cell line and spheroids culture

The U87mg Luc+ human glioma cells were cultured in Dulbecco's Modified Eagle Medium, supplemented with 10% (v/v) of Fetal Bovine Serum (FBS), Glutamax, and 1% (v/v) of Pen-Strep solution. Tumor spheroids were obtained by seeding 1.25×10^4 cells/ml into ultra-low attachment (ULA) 96-well round bottom plates (200 μL/well). All cells and spheroids were handled under aseptic conditions and incubated at 37°C in a 5% CO_2 atmosphere.

METHOD DETAILS

CLM sample preparation and imaging

The day before imaging, the spheroids growth medium is replaced with glucose-free medium to induce cell starvation and prepare the spheroid for [^{18}F]FDG uptake. Before imaging, the spheroid is incubated for 60 min at 37°C in a 200 μL glucose-free medium solution containing 5 MBq [^{18}F]FDG. Subsequently, it is washed three times for 2 min with non-radioactive medium. Following uptake and washing, the spheroid is withdrawn from the well using a pipette with a cut tip and transferred onto a microscope slide. A drop of growth medium is also transferred on the slide and prevents spheroids from drying out in case of prolonged exposure. No coverslip is used to avoid compression of the spheroid and consequent shape aberrations or oxygen deprivation. After focusing the spheroid in bright field mode, the door of the light tight box is closed, and a blackout fabric is placed on the box to stop light possibly filtrating through fissures. To have an as dark as possible environment, the room lights are turned off.

BLM sample preparation and imaging

The procedure for BLM is similar to the one described in the previous section for CLM, but it is inherently simpler. Since the cell line used is already luciferase-tagged, a brief incubation with luciferin is sufficient to trigger the bioluminescence reaction, provided the cells are alive and oxygen is present. For imaging, 50 μL of luciferin 15 mg/mL solution (D-Luciferin Firefly, potassium salt diluted in PBS) are added to 200 μL of growth medium, in which the spheroid has been seeded, and the mixture is incubated for 1 min. Following incubation, the spheroid is immediately retrieved from the well and transferred onto a microscope slide, without the need for washing.

Spheroids paraffin inclusion, sectioning and staining

Spheroids were fixed in 4% paraformaldehyde (PFA) for 40 min at room temperature, followed by three washes in phosphate-buffered saline (PBS). To facilitate handling during processing, spheroids were embedded in 2% agarose prepared in PBS. Samples were then transferred to 70% ethanol and stored overnight at 4°C in embedding cassettes. The following day, the samples were dehydrated through graded ethanol, followed by incubation in xylene. Paraffin infiltration was carried out in an oven at 56°C for 45 min, repeated twice. Spheroids were then rapidly embedded in paraffin molds, and the blocks were cooled at −20°C prior to sectioning. Sections of 7 μm thickness were cut using a microtome, mounted onto glass slides, and incubated overnight at 37°C to ensure proper adhesion. After deparaffinization, the sections were stained with hematoxylin (2 min) and eosin (1:10 in water, 30 s). Following dehydration, the slides were cleared in xylene, mounted, and coverslipped.

QUANTIFICATION AND STATISTICAL ANALYSIS

Spheroids activity evaluation

To evaluate the radiopharmaceutical uptake of the spheroids, they were transferred into a test tube for counts per minute (cpm) measurement using a γ-counter (LKB Wallace 1282 Compugamma - PerkinElmer). The cpm values were corrected with an exponential decay factor to account for the time elapsed since incubation. Subsequently, these values were converted to disintegrations per minute (dpm) by applying the γ-counter efficiency factor and finally expressed in kilobecquerels (kBq).

Image processing

All original images exhibited individual pixels or small clusters of high-intensity pixels, caused by gamma rays emitted from the decay of the radiopharmaceutical present in the sample, and in some cases by cosmic rays interacting with the CCD sensor. These artifacts were removed through a denoising process performed with ImageJ prior to further analysis. Subsequently, all images were corrected for bias, dark current, and background signals. The bias in a CCD camera is a DC offset added to all pixel values to prevent negative numbers. It was measured by averaging 50 frames acquired with an exposure time of 10^{-6} s and the shutter closed. The dark current signal, generated by thermal noise within the CCD, is typically negligible in a cooled camera. However, certain pixels, known as hot pixels, can still display abnormally high dark current. To correct for this, five dark images were acquired at −80°C with a closed shutter and an exposure time of 300 s. A sigma clipping algorithm was applied to eliminate any residual cosmic ray artifacts, and the resulting frames were averaged to enhance the signal. A hot pixel map was then generated from this average image and used to correct both background and luminescence images by replacing each defective pixel with the mean of its surrounding neighbors. To evaluate the background signal, a series of images with the same settings but with an open shutter were acquired. After averaging (with sigma clipping), the bias image was subtracted from the result to obtain the corrected background. All correction steps were implemented automatically using a custom Python script.

Image features quantification and statistics

Quantification of spheroid features, including area, average signal, and integrated signal, was carried out by manually selecting each spheroid in ImageJ. The resulting measurements were collected and imported into a pandas DataFrame for further analysis in Python. To assess differences between irradiated and non-irradiated spheroid groups, one-sided Mann–Whitney U tests were performed using the scipy.stats library. Correlation matrices were computed using the pandas.corr() function with the Pearson method.

Signal-to-noise and contrast-to-noise ratios

Signal-to-noise ratio (SNR) and contrast-to-noise ratio (CNR) were computed for images in section results. The mean and standard deviation (STD) of the pixel values were calculated in two regions of interest (ROIs) of each image: one in the center of the ^{22}Na source (signal, SGN) and one outside the source (background, BG). The Signal-to-Noise Ratio (SNR) was calculated as the ratio of the mean of SGN to the standard deviation of BG. The Contrast-to-Noise Ratio (CNR) was calculated as the difference between the mean of SGN and the mean of BG, divided by the STD of BG.

Monte Carlo simulations of Cerenkov emission

To compare the Cerenkov emission of different radionuclides, a Monte Carlo simulation was performed using the TOPAS MC Tool for Particle Simulation. A 2 mm-long glass capillary with an internal diameter of 1 mm and an external diameter of 1.5 mm was simulated and filled with water. 10^7 events of radioactive decay were randomly generated within the liquid, and a phase-space scorer was employed to count the number of optical photons reaching the external surface of the cylinder. The space surrounding the capillary was set to lead, immediately halting the photons paths upon contact with the surface. To simulate the distribution of Cerenkov photons, the x-z plane bisecting the capillary was used as a phase space scorer. The coordinates of each Cerenkov photon intersecting this plane were recorded and mapped onto a 256 × 256 matrix. Each time a photon landed within a specific square region of the matrix, the corresponding pixel count was incremented, building a reconstruction of the 2D spatial distribution of the emitted photons. The included physics modules were g4em standard opt0, g4radioactivedecay and g4optical. In the supplemental information (Figure S3) a graphical representation of the simulated geometry is shown.